Simulation of stress-assisted localised corrosion using a Cellular Automaton Finite Element approach

FATOBA, O.O., LEIVA-GARCIA, R., LISHCHUK, Sergey <http://orcid.org/0000-0002-9989-765X>, LARROSA, N.O. and AKID, R.

Published version

FATOBA, O.O., LEIVA-GARCIA, R., LISHCHUK, Sergey, LARROSA, N.O. and AKID, R. (2018). Simulation of stress-assisted localised corrosion using a Cellular Automaton Finite Element approach. Corrosion Science, 137, 83-97.

Copyright and re-use policy

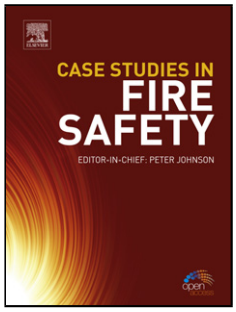

Title: Simulation of stress-assisted localised corrosion using a Cellular Automaton Finite Element approach

Authors: O.O. Fatoba, R. Leiva-Garcia, S.V. Lishchuk, N.O. Larrosa, R. Akid

PII: S0010-938X(17)31914-5
DOI: https://doi.org/10.1016/j.corsci.2018.03.029
Reference: CS 7445

To appear in:

Received date: 23-10-2017
Revised date: 1-3-2018
Accepted date: 16-3-2018

Please cite this article as: Fatoba OO, Leiva-Garcia R, Lishchuk SV, Larrosa NO, Akid R, Simulation of stress-assisted localised corrosion using a Cellular Automaton Finite Element approach, *Corrosion Science* (2010), https://doi.org/10.1016/j.corsci.2018.03.029

Simulation of stress-assisted localised corrosion using a Cellular Automaton Finite Element approach

O. O. Fatoba [a],
R. Leiva-Garcia [a],
S. V. Lishchuk [a,b],
N. O. Larrosa [c],
R. Akid[a]

[a] *Corrosion and Protection Centre, School of Materials, University of Manchester, Sackville Street, Manchester M13 9PL, UK.*
[b]*Materials and Engineering Research Institute, Sheffield Hallam University, Howard Street, Sheffield S1 1WB, UK.*
[c]*Faculty of Engineering, University of Bristol, University Walk, Clifton BS8 1TR UK.*

Highlights

- Stress-assisted localised corrosion is simulated using cellular automata finite element approach.
- Localised corrosion component of the damage is modelled using cellular automata.
- Stress concentration effect of pit geometry is analysed using finite element method.
- A feedback loop between the cellular automaton and finite element models allows simulation of stress-assisted localised corrosion.
- Comparison of simulation results with experimental measurements show good agreement.

ABSTRACT

In this paper, the overall corrosion damage process is modelled sequentially using cellular automata (CA) to describe the localised corrosion component, and finite element analysis (FEA) to account for the mechanical component resulting from the stress concentration effect of the corrosion defect (pit). Synchronous execution of the CA and FEA, and provision of feedback between both provides a good approximation of stress-assisted pit development. Qualitative and quantitative comparison of simulation results with experimental measurements show good agreement. In particular, the model shows that mechanical effects, notably plastic strain, accelerates the rate of development of localised corrosion.

Keywords: A. Low alloy steel; B. Potentiostatic polarisation; B. Cellular automata; B. Finite Element analysis; B. Modelling studies; C. Pitting corrosion.

1. Introduction

Pitting corrosion is a destructive form of localised corrosion, which can lead to failure of engineering components that are subject to simultaneous mechanical loading and a corrosive environment [1-4]. In these applications, pitting corrosion presents a limitation to the structural integrity as pits can act as initiation sites for fatigue and stress corrosion cracks, leading to accelerated fracture and reduction in service lifetime with potential catastrophic consequences [3-8]. From the design and reliability point of view, the development of a multi-stage model capable of predicting stress-assisted pitting and subsequent cracking is of great value for structural integrity management of components and structures.

Classic pitting corrosion damage is associated with the localised dissolution of the metal substrate caused by a breakdown of the protective surface film and has been widely investigated [9-12]. As the material employed in this study is carbon steel, it is worthy of note that in contrast to classic pitting corrosion, which involves the breakdown of passive film on metals, carbon steel can undergo pitting corrosion under certain conditions, such as those found in oil and gas environments [13, 14]. Here, the pitting corrosion process is associated with the local breakdown of the iron carbonate and/or iron sulphide scales that are formed on the internal surface of the linepipe, thus resulting in localised dissolution of the underlying substrate and formation of corrosion pits [15, 16]. Pitting corrosion damage and associated mechanisms in the oil and gas environment has been previously reviewed in [16-19].

In broad terms, the pitting process evolves through three main stages, namely, nucleation, metastable growth and stable growth [20-22]. The nucleation stage usually involves passive film/protective scale breakdown due to, for example, point defects in the passive film, physical and chemical metal surface inhomogeneities, such as inclusions, grain boundaries and precipitates, and film damage from mechanical stress [12, 23-25]. During the metastable stage nucleated pits can repassivate, thus becoming dormant. Subject to material/environment conditions these pits may reactivate and continue to grow, becoming stable pits. The kinetics of pit growth (dissolution) during the stable growth stage is controlled by several factors including; mass transport of corrosion species, hydrolysis, and precipitation and accumulation of corrosion products. Although pitting corrosion damage has been widely investigated [9-12], models presented in the literature tend to be empirical, phenomenological and deterministic in nature [26-30] and

computational modelling of local corrosion damage remains a challenge. This is due to there being several coupled time-dependent and stochastic chemical-physical processes, all operating at different length scales (macroscopic, mesoscopic, microscopic) and time scales [31]. The damage process is further complicated when the material is subject to mechanical loading wherein the local stress and strain concentration around a progressively changing pit geometry can accelerate the pitting process [32, 33]. Therefore, the formulation of a model capable of predicting such a complex system will involve multi-scale analysis both in time and space.

Early efforts directed at modelling pitting corrosion largely focused on the formulation of empirical laws based upon laboratory and/or in-service pit growth rate measurements. The literature relating to these empirical models was reviewed by Szklarska-Smialowska [12]. Turnbull [34], later commented that the limitation of existing models is the lack of mechanistic content, as only average properties representing macroscopic behaviour of the system are measured. Later efforts attempted to address this limitation through the development of more realistic, mechanistically-based, atomistic models which use theoretical principles and partial differential equations to interface the electrochemical processes controlling pit growth kinetics [26, 27, 35, 36]. Further, they are also limited by complexity, the stochastic nature of the corrosion process, and a lack of appropriate input data restricting their application. Advances in computational capabilities have recently enabled the simulation of pitting corrosion behaviour using new modelling paradigms at the mesoscopic scale such as Monte Carlo [28, 37], artificial neural networks [29, 38] and cellular automata [39-41]. The focus of the work presented in this paper is on this latter approach, cellular automata modelling.

Cellular automata (CA) are discrete computational systems where the future state of each cell in the modelling space is determined by the current state of the cell and that of its neighbourhood cells based on local transformation rules [30]. In contrast to partial differential equations, in which space, state and time are continuous, these three, and other dynamic variables, are discrete in CAs [39, 42]. All the cells have access to the same set of states at any time step and can assume only one of a finite number of possible states. Based on the local transformation rules, which apply to all the cells in the automaton and are applied through a number of discrete time steps, all cells are updated synchronously so that the system evolves in

an iterative manner. The physical metal-environment system can be discretised into a metal/film/electrolyte cellular lattice of sites (also referred to as 'cells'), where each of the cells in the lattice can represent different species taking part in the corrosion process. CAs are increasingly being applied to model localised corrosion in various material-environment systems due largely to their ability to simulate electrochemical processes, and their stochastic nature, at a mesoscopic scale [40, 41, 43].

Results from investigations carried out by Malki and Baroux using the cellular automota technique [37] showed that metal dissolution rate and IR drop, modelled using a dissolution probability and via a linear potential gradient that relates the pit depth to dissolution probability respectively, have a strong influence on corrosion pit growth kinetics. Wang and Han employed cellular automaton modelling combined with finite element analysis to investigate the effect of applied stress on metastable pitting corrosion [44, 45]. A higher growth rate of metastable pitting for both single and double pits was observed under the influence of stress compared to stress-free conditions. Li and co-workers [46, 47] also simulated the growth of metastable pits and their transition to stable pitting in stainless steel and demonstrated that the time dependence of pitting current follows the $I = f(t^2)$ law. Van der Ween [48] developed a cellular automaton model to simulate pitting corrosion in a bimetallic material. They observed differences in the number of initiated pits and the growth rates of pits in different chloride concentrations. The influence of various electrochemical parameters on the pitting initiation and growth behaviour in aluminium was investigated by Pidarparti et al [49] using cellular automaton simulation.

While these studies show that the nature of electrochemical processes, wherein the state of the species in corrosion reactions changes as a result of interaction with other species around it, makes CA a convenient tool for simulating the metastable and stable growth stages of localised corrosion, to date, the simulation of stable pit growth involving mechanical loading has with perhaps the exception of the work of Wang and Han, on metastable pitting [44], not been reported in the literature. The aim of this work is to investigate the growth of local damage under the influence of applied stress using a cellular automaton.

In this paper, a CA model has been coupled with finite element modelling (Cellular Automoton Finite Element (CAFE)), in order to simulate the physical damage occurring due to the interactions between corrosion and mechanical stress, which takes place during the early stages of environment assisted

cracking. The objective, therefore, of the study is to explore the applicability of this type of hybrid model to simulate stress-assisted pit development, applicable to the mechanisms of stress corrosion cracking and corrosion fatigue. The CAFE model has adjustable parameters, which correlate with physical processes and may be calibrated based upon experimental data. Simulations were carried out to investigate the influence of various electrochemical parameters that control pit propagation kinetics, applied stress, and flow on the local corrosion kinetics and evolution of pit characteristics. The results obtained from experiments are compared with the output of the CAFE model.

2. Experimental

Tests were carried out on American Petroleum Institute (API) 5L X65 steel, supplied as pipe sections. The material is a high-strength, low alloy steel employed in oil and gas applications. The chemical composition is given in Table 1. The 0.2% proof strength, ultimate tensile strength and elongation of the steel are 524 MPa, 614 MPa and 31% respectively [50]. Metallographic analysis showed that the microstructure is composed mainly of pseudo-polygonal and equiaxed ferrite grains.

Electrochemical-mechanical tests were conducted to simulate stable pit growth in 0.6 M NaCl, pH 6.2, using two different configurations. In the first series of tests, a 3-electrode micro-capillary cell (Figure 1), consisting of a 500 μm diameter capillary pipette, was employed to investigate pit growth under non-flow and unstressed conditions. The second configuration, which was employed to investigate the effects of applied stress and flow on pit growth, consists of a 3-electrode scanning droplet system and a 2 kN computer-controlled hydraulic machine, both mounted on a Uniscan Electrochemical Workstation (Figure 2). The flowing solution feature of the scanning droplet system was employed for studying the effect of flow on localised dissolution rates. A steady laminar flow rate of 0.02 mL/s was maintained during testing via a peristaltic pump. Testing involved the simultaneous application of a cyclic stress of $\sigma_{max} = 200$ MPa to the test sample (Figure 3), at a stress ratio and frequency of 0.1 and 2 Hz respectively, during polarisation. These conditions were chosen as they typically represent an oil and gas linepipe, where there is a positive stress ratio due to the internal pressure resulting from the pipe contents and a low cyclic fluctuation (frequency) of the line pipe typical of seawave action. In all the tests, a potential of 1V vs

Ag/AgCl, above the open circuit potential, was applied in potentiostatic mode for different times, after which specimens were cleaned to remove corrosion products from the pit, and the pit morphology was characterised using a Keyence VK-X200K 3-D confocal microscope. The determined output characteristics for the time evolution of pitting behaviour are maximum pit depth, pit aspect ratio (ratio of pit depth to half pit width) and pit morphology.

3. Experimental results and discussion

An example of an artificial pit created on the fatigue test specimen is shown in Figure 4a. Analysis of the cross-sectional profiles of all the pits generated in this study generally showed a pseudo-hemispherical shape (Figure 4b). Hence the theoretical pit depth corresponding to each time scale was estimated from the current-time measurements using Faraday's law and assuming a hemispherical pit shape with a radius that is equal to half of the experimentally measured pit width.

Measurements of maximum depth of pits, taken at different polarisation times, without flowing solution and the application of stress, compared with theoretical estimates are presented on a log-log plot in Figure 5a while aspect ratios are shown in Figure 5b. It can be observed that both pit depth and pit aspect ratio increase with time. Although the theoretical data, derived from the measured pit current density and applying Faraday's law, shows a slight overestimation of the experimental pit depths, the correlation between both is considered to be good. The rate of change in pit depth decreases with time and can be represented by an empirical power law relationship of the type $d_p = A\, t^{\beta}$ where d_p is pit depth (μm), t is time (hours), and A and β are constants, in the case of Figure 5a, being106 and 0.46 respectively. The decrease in pit growth rate is attributed to a diffusion-control mechanism whereby the mass transport of corrosion products away from the pit site is limited thus leading to corrosion product accumulation inside the pit. This results in the creation of a diffusion barrier between electrochemical species across the metal-electrolyte interface, limiting the anodic dissolution process [26, 51] and consequently the pit growth rate. Whilst stagnant, non-flow, conditions, limit mass transport of cathodic species (dissolved oxygen) to the reaction sites within the pit and reduce the pit growth rate [52], this possibility is excluded because at the applied polarisation potential, the majority of the cathodic reactions take place on the counter electrode.

The influence of solution flow (at 0.02 mL.s^{-1}) on pit growth rate is shown in Figure 6, where the depth-time relationship can be described by a power law relationship, the values of the parameters *A* and *n* being higher than for non-flow conditions. This indicates that at any given time, pits were deeper under flow compared to non-flow conditions. This effect of flow can be attributed to diffusion control. In contrast to stagnant conditions, the advection effect of flow facilitates the mass transport of the cathodic reactants to the pitting site and the corrosion products away from the pit. Consequently, the metal dissolution process is accelerated leading to increased pit depth, for a given time, over that under non-flow conditions. Also shown in Figure 6 is the influence of applied cyclic stress of $\Delta\sigma$ = 180 MPa on pit growth rate at a flow rate of 0.02 mL.s^{-1}. The observation noted here, is of increasing pit size with increasing stress, and is consistent with the results from previous studies [32, 53-55]. While the applied stress range is in the elastic region of the material, depending on the pit depth, the stress concentration effect of the pit can give rise to plastic strains around the pit [56-58]. This results in increased localised electrochemical activity [53, 55] as local activity of dislocations at the pit site is promoted due to a lower activation energy being required to remove atoms of higher energy state [59].

4. Cellular Automata Finite Element Modelling

In the current work, a cellular automata finite element (CAFE) modelling approach has been developed for simulating stress-assisted pitting corrosion at a mesoscopic scale. The CAFE model decouples the cumulative damage process into localised corrosion and mechanical components. In the first stage, a semi-probabilistic cellular automaton (CA) is used to model the localised loss of metal (in this case pitting). As discussed above, pitting corrosion is a complex phenomenon and a simultaneous study of all the parameters, and their interactions, involved in the process is a complex and challenging task. For this reason, the CAFE model developed in this work focuses on the principal processes of metal dissolution, metal ion hydrolysis, diffusion of corrosion species and mass transport of corrosion products. A schematic showing an overview of the CAFE model architecture and development procedure is shown in Figure 7. The model enables the simulation of the complex interactions between these physical and electrochemical processes. The local stress and strain distribution around the pit, resulting from the deformation of the cellular structure, are analysed using finite element analysis (FEA). The coupling of the two mechanisms

is made by (i) changing the geometry of the cellular structure in the FE model as a result of dissolving cells (corrosion) determined by CA, and (ii) changing the dissolution kinetics in the CA model based on the local stress and strain determined by FEA, as damage progresses with time. Concurrent execution of the two analyses with provision of a feedback loop between them provides a good approximation for simulating the interaction between corrosion and deformation effects and studying the effect of applied stress on pitting corrosion development in the early stages of environmentally assisted fracture.

4.1. Configuration of cellular automata

The CA modelling space was setup in a manner that mimics the pitting corrosion process in a real system and allows the simulation of the experimental microcell tip-electrolyte-metal interface (see inset in Figure 1), the schematic representing the real system is shown in Figure 8. As can be seen in Figure 8a and 8b, the region of interest is the interface between the metal substrate, electrolyte and the walls of the capillary. Hence a section of the scaled surface (Figure 8c) equivalent to the width of the capillary tip, was omitted in order to mimic this interface.

A two-dimensional lattice space consisting of 2000 x 1000 (i x j) cells, shown schematically in Figure 9, was employed for simulations. The upper half of the lattice space (i.e. i = 1 to 1000) represents the aqueous solution containing the corrosive species while the lower half (i = 1001 to 2000) represents the metal structure. A Moore neighbourhood (Figure 10), which considers all the eight neighbours of an objective cell, was adopted in the CA model, as it is considered to simulate electrochemical processes more realistically. The cells, represented as squares with dimensions of unity, are not to be associated directly with atoms, anions or cations, as the model is mesoscopic. A more realistic interpretation is that of a homogenous grouping of these corrosion species in order to capture electrochemical behaviour. The cells in the boundaries of the metal domain in the modelling space are excluded from participating in electrochemical processes. In order to simulate the physical size of the capillary tip of the electrochemical cell (500 µm – Figure 8), the CA lattice space was scaled up by a factor of 2.5 so that a CA cell size is equivalent to 2.5 x 2.5 µm. This means that 20 CA cells are equivalent to the capillary tip of the corrosion cell being simulated. This cell size was fixed throughout the CA computations.

4.2. Electrochemical system

The CA model is developed for an iron-water electrochemical system. Non-hydrated forms of corrosion products such as magnetite (Fe_3O_4) or iron (ferric) oxide (Fe_2O_3) are excluded. Only the five species that have a stable area on the iron-water Pourbaix diagram at 25^0C, notably, Fe, Fe^{2+}, Fe^{3+}, $Fe(OH)_2$ and $Fe(OH)_3$, are considered in the selection of the states that the cells can exist in the cellular automata system. The electrochemical reactions for these five species are illustrated in Equations 1 to 4. The eight different sites and states that each cell can assume in the model are given in Table 2 and illustrated schematically also in Figure 8, where the sites designated as '**C**' represent both the capillary wall in Figure 8a and the capillary surface in Figure 8b.

$$Fe \leftrightarrow Fe^{2+} + 2e^- \quad (1)$$

$$Fe^{2+} \leftrightarrow Fe^{3+} + e^- \quad (2)$$

$$Fe^{2+} + 2H_2O \leftrightarrow Fe(OH)_2 + 2H^+ \quad (3)$$

$$Fe^{3+} + 3H_2O \leftrightarrow Fe(OH)_3 + 3H^+ \quad (4)$$

4.3. Evolution rules of cellular automata

The algorithm for the CA model was written with Matlab® programming software [60]. The model was implemented in two parts: a corrosion loop, which simulates the electrochemical reactions, and a diffusion loop, which simulates the diffusion of species within the solution during the electrochemical damage process. In the CA model, a site can only be occupied by a single state at any given time. For example, **R** and **P1** sites cannot occupy the same site at the same time as they are in different states.

4.3.1. Rules for corrosion reactions

The rules for the corrosion reactions are classified into four groups based on Equations 1 – 4. The forward reaction for oxidation of Fe to Fe^{2+} (Equation 1) takes place with a corrosion probability ***P_corr*** when at least one acidic site **H** is in the neighbourhood of a metal site **M** (Figure 11a); the **M** site will be replaced by an **R** species. When at least one acidic site **H** is in the neighbourhood of reactive metal site **R** (Figure 11b), oxidation of Fe^{2+} to Fe^{3+} (Equation 2) takes place with oxidation probability ***P_ox***; the **R** site will be replaced by a **D** species. When at least two of the neighbours of a reactive metal **R** are neutral sites **W** (Figure 11c), hydrolysis of Fe^{2+} to $Fe(OH)_2$ (Equation 3) takes place with hydrolysis probability

P_Hyd*1**; the **R** and two **W** sites are replaced with **P1** and two **H** species respectively. The final reaction involves the hydrolysis of Fe^{3+} to $Fe(OH)_3$ according to Equation 4, when at least three neighbours of a **D** site are neutral sites **W**. The reaction will take place with hydrolysis probability ***P_Hyd2 (Figure 11d) and the **D** and three **W** sites will be replaced by **P2** and three **H** species respectively.

4.3.2. Rules for diffusion

It is well known that pit growth kinetics is largely governed by diffusion-control [61, 62], hence it is important to consider the diffusion of electrochemical species in the simulation model. The five diffusible species considered in the CA model and their associated probabilities are: Fe^{2+} [***P_diffFeII***], Fe^{3+} [***P_diffFeIII***], $Fe(OH)_2$ [***P_diffFeHyII***], $Fe(OH)_3$ [***P_diffFeHyIII***] and H^+ [***P_diffH***]. Each of these species will diffuse according to their corresponding probabilities, shown in brackets. The diffusion of species, except $Fe(OH)_2$ and $Fe(OH)_3$, are assumed to be isotropic, implying that such diffusing species can move in any direction with similar probability (Figure 12a). In the case of the hydroxides, while $Fe(OH)_2$ can exist as both a solute and solid precipitate, $Fe(OH)_3$ is insoluble in water. For the insoluble forms of these hydroxides, it is assumed that the probability of moving in a downward direction due to gravity will be greater than in any other direction (Figure 12b) thus resulting in tendency for corrosion product accumulation. This effect was accounted for by defining a *sedimentation factor*, ***Sed***, in the case of the hydroxides, and implemented by multiplying both [***P_diffFeHyII***] and [***P_diffFeHyIII***] by *Sed* in the diffusion loop. This sedimentation factor has a dual role; accounting for the precipitation of the hydroxides and for the decrease in the rate of precipitation of the hydroxides when flow is present. The later indirectly shows the effect of flow on the pitting process as convection is not explicitly modelled. It is recognised that the influence of convection i.e. displacement of corrosion species will be far greater than that of diffusion. Further discussion on this is presented later.

The diffusion of species is also dependent on the individual diffusion coefficients. Some authors [63, 64] have previously modelled diffusion of species in CAs fairly accurately by means of a random walk process. A similar approach was introduced in this work wherein the potential walkers are the diffusing sites **[H]**, **[R]** and **[D].** The CA includes several diffusion steps for each corrosion step. Species with relatively higher diffusion coefficients have higher mobility thus will move through dimensionally longer

distances in the simulated space compared to those with lower coefficients. The diffusion rules was simplified by relating diffusion distances to diffusion coefficients of the Fe^{2+}, Fe^{3+} and H^{+} (0.719 x10^{-9}, 0.604 x10^{-9} and 9.3 x10^{-9} m^2/s respectively). Therefore the H^{+} represented as the acidic sites have higher mobility compared to the Fe^{2+} and Fe^{3+} species.

It is recognised that the kinetics of anodic dissolution during stable pit growth can be strongly influenced by IR drop [65, 66]. In real systems, the effect of IR drop is related to a complex set of laws that are dependent on several variables not limited to solution conductivity and distance between cathodic and anodic sites (which change the distance of the electron flow). Some authors [37, 48] have considered IR drop by incorporating a linear gradient potential parameter, Φ, which relates the dissolution probability to pit depth in the form:

$$P\_ox = P\_ox_0\left(1 - {\Phi d_p}/{d_m}\right) \quad (5)$$

where P_ox is the dissolution probability under a potential gradient (active IR drop $\Phi \neq 0$), P_ox_0 is dissolution probability with no IR drop ($\Phi = 0$), d_p is pit depth, and d_m is a scale constant equivalent to the total depth of the metal layer in the modelling space.

In the simulated capillary system with a concentrated brine solution, there is an accumulation of corrosion products at the tip of the cell. As the pit depth increases, this has a strong effect on the localised corrosion behaviour as active sites are hindered from participating in electrochemical activity. Therefore, the IR drop was not taken into account because with the increase in the size of the pit, the effect of the corrosion product accumulation has a dominant effect as the system is under diffusion control.

4.4. Finite Element Modelling

4.4.1. Finite element analysis of pit geometry

The localised stress and strain distribution around the pit geometry, resulting from the CA, was analysed using FEA. Preliminary analysis of the model results revealed that pit depth can remain constant for up to ten consecutive time steps, hence it was considered unnecessary to re-calculate stresses and strains at every time step during the simulation. Therefore FEA of the pit geometry was performed after every five CA time steps. An algorithm that interfaces the CA model with ABAQUS® FEA

software [67] was developed using Matlab® scripting language [60]. The script converts the output matrix from the CA into a solid part, creates and assigns material properties (stress-strain test data of X65 steel [50]) to the part, and creates an assembly of the part and analysis steps for the simulation. It also applies boundary condition by restricting the elements on the left edge of the metal matrix from rotation and displacement (see Figure 9) and refines the mesh around the pit. In order to minimize the computational time for stress analysis while ensuring accuracy of the FEA results, a mesh size study was conducted. Based on the results, a finer mesh size equal to twice the cell size (5 x 5 μm) was chosen for the mesh around the pit while away from the pit, a coarse mesh of 5 x 200 μm was chosen. The cyclic stress (fatigue component) was not directly simulated in this work, rather it was indirectly introduced in the FE model as a tensile load. This applied tensile load in the FE model is equivalent to the maximum stress that was applied during fatigue cycling (200 MPa). This approach was adopted due to two reasons. Firstly, whilst the stress cycle and the CAFE algorithm essentially have different time scales, the influence of frequency is effectively built into the CAFE model, that is, on each CA loop the effect of stress is incorporated in the resulting values of the CA probabilities. Secondly, whilst recognising that the stress waveform is a factor that may influence the fatigue crack growth rate in the presence of a corrosive environment [68, 69], in the current study, no cracks are formed from the pit and therefore the model deals only up to the pit-crack transition. Secondly, a previous study reported that no significant differences in corrosion rates were observed at stress levels below the yield stress when the maximum stress in the cyclic load was similar to the tensile stress [70]. In the current model, the applied stress (200 MPa) is below the yield strength of the material. In this respect we do not believe that there is will be any significant effect of the waveform on the magnitude of stress-assisted corrosion.

Boundary conditions and loads must be applied to continuous surfaces during FE analysis; hence it was necessary to ensure that the cells in the boundaries of the metal space do not corrode. This was achieved by excluding the boundary cells in the metal space from the corrosion process. The element types assigned to the model were bilinear 4-node quadrilateral plane strain (CPE4) continuum elements. The final step is the creation of an input file, which is submitted to the ABAQUS standard solver for analysis. From the resulting output database (.odb file), a script written in Python was used to output the

components of the stress, total strain and plastic strain tensors at all integration points associated with each element. These components were used to evaluate the inputs into the mechanical-electrochemical model employed to account for the effect of stress on corrosion, as described in the next section.

4.4.2. Rules for mechanical-electrochemical effect

It has been shown that anodic dissolution of metals and alloys can be promoted by deformation [55, 71, 72] and that applied stress can increase pit growth rates [33, 73]. In this study the mechanical-electrochemical interaction has been modelled adopting the Gutman model, which is based on bulk thermodynamic analysis of metals [74, 75]. The model has previously been employed by some researchers to account for the effects of mechanical stress and strain on corrosion kinetics [44, 76]. During strain hardening, the equation for anodic dissolution due to deformation can be determined from;

$$I/I_n = exp\left(\frac{\Delta P V_m}{RT}\right) \quad \textit{Elastic deformation} \tag{6}$$

$$I/I_n = \left(\frac{\Delta\varepsilon}{\varepsilon_0} + 1\right) exp\left(\frac{\sigma_m V_m}{RT}\right) \quad \textit{Plastic deformation} \tag{7}$$

where I is the anodic current resulting from deformation, I_n is the anodic current for no deformation, ΔP is the hydrostatic pressure, V_m is the molar volume, $\Delta\varepsilon$ is the equivalent plastic strain, ε_0 is strain at onset of strain hardening, σ_m is the hydrostatic stress, R is the gas constant and T is the temperature.

These parameters, evaluated from the stress and strain components described in the previous section, were used to evaluate the *influence factor*, I/I_n, which will be greater than unity in regions in the metal matrix having localised stress and strain. The standardised constants used in the model at a temperature of 25^0C are: T = 298 K, $V_m = 7.0923\times10^{-6}$ $m^3.mol^{-1}$ (for iron), and R = 8.314 $m^2\,kg\,s^{-2}\,K^{-1}\,mol^{-1}$. The strain at on-set of strain hardening i.e. yielding is taken as 0.2%.

The *influence factor* was evaluated for each element in the FE model. Since each element in the FE model is equivalent to each cell in the CA model, the stress effect on corrosion was accounted for by modifying the state of the metal lattice. The modification is achieved by multiplying the oxidation probability **[*P_corr*]** by the *influence factor*. Since this factor is always greater than or equal to unity, the tendency for corrosion in regions with increased local stress and strain in the metal matrix increases correspondingly from the base state to a more reactive state.

4.5. Optimization of CAFE model

The advantage of the CAFE model lies in its ability to simulate, with reasonable accuracy, the time-dependent evolution of pit geometry and the associated strain distribution in the vicinity of the pit. This will be dependent on the individual values of the input parameters in the model. One means by which these values may be calibrated is by comparing the simulation results with experimentally determined pit growth data. Since the model possesses several input parameters, the CA model possesses a complicated error surface in the parameter space hence optimization is necessary in order to obtain a set of input probability values, which globally minimises the error between model results and experimental data. From a modelling standpoint, pit depth is the most generally used parameter for describing pitting behaviour hence the mean square error (MSE) between the simulated and experimentally measured maximum pit depth as a function of time is chosen as the objective function to be minimized during the optimization process. The optimization method used in this work to minimize the MSE is similar to a grid search using a Sobol sequence [77]. The model was optimized using the two sets of experimental data that were obtained from tests with and without flowing solution (see Figures 5 and 6). It should be noted that only the experimental data obtained under flowing without the application of stress was employed for optimization since the objective is to determine the optimum values of the CA model input parameters. This optimized CA model was then employed for simulating stress-assisted pit growth.

For the optimization procedure, the following steps were followed in the optimization algorithm. Firstly, in order to determine a starting point for the optimization process, a preliminary series of simulations were run manually using combinations of values that were assigned randomly to all the nine input probabilities in the CA model. Although these initial values have been described as random, the values chosen were deemed to be within limits of physical relevance. Thereafter, the combination of parameters that resulted in the best time series evolution of the pit depth relative to the experimental data, based on visual inspection, were provided as inputs parameters for the optimization algorithm. In addition, ranges of values representing the search space for each of the input probabilities was also specified. In order to be able to implement a Sobol sequence, the CA model parameters were first divided into three groups, namely, group 1 (*P_corr* [0.1 – 0.9], *P_ox* [0.1 – 0.9], *Sed* [0.1 – 8]), group 2 (*P_Hyd1* [0.1 – 0.6],

P_Hyd2 [0.1 – 0.6]) and group 3 (*P_diffH* [0.1 – 0.9], *P_diffFeHyII* [0.02 – 0.09], *P_diffFeHyIII* [0.02 – 0.09]). In the optimization algorithm, several combinations of the three parameters in group 1 are chosen from their subranges (given in their respective adjacent square brackets) using a Sobol sequence while the other two groups are fixed with constant values. For each combination of values, the maximum pit depth evolution with time is determined, after which the MSE is calculated with reference to the experimental data at specified intervals of the time series. Since the CA model is stochastic in nature, model simulations using the parameter combinations that minimize MSE are performed fivefold in order to account for this stochasticity. The results from these five repetitions are then averaged and again the MSE is calculated, after which the probability values that result in the lowest average MSE is selected as the optimal solution. It should be noted that, due to equifinality, different probability value combinations can result in similar results [78].

Next, the optimized values for group 1 parameters and the preliminary values for group 3 parameters are set as constants while the same sequence described above are followed. This is also repeated for the group 3 parameters in turn. It should be noted that the main difference between two sets of experimental conditions being simulated is the effect of the flow, which reduces the precipitation of corrosion species, as new fresh solution is pumped into the electrochemical cell. This effect is simulated exclusively by effectively reducing the value of the sedimentation factor (Sed). Therefore the CA model with flowing solution was optimized by varying only *Sed* while keeping the values of the other input parameters that were obtained from the CA model without flowing solution constant. The obtained optimum parameters for flowing and non-flowing solutions are given in Table 3.

5. Modelling results and discussion

In this section, simulation results obtained from both the CAFE model and experiments are reported and discussed, adopting a suitable timescale calibration in the CAFE model. The chosen quantitative and qualitative comparison parameters are; maximum pit depth, pit aspect ratio, and pit morphology. In the model, the maximum pit depth is the numerical difference between the row containing the deepest corroded cell and that of the surface of the metal lattice.

5.1. Evolution of pit characteristics with time

For both CA models simulating stable pit growth under non-flow and flow conditions, one time step corresponds to 5.51 seconds. Figure 13 presents the simulation results for maximum pit depth as a function of time under stagnant and flowing conditions. The predicted cross-sectional profiles of pits, compared with those obtained from experiments at different time intervals, are shown in Figure 14. Comparisons between the simulation results and experimental data presented in Figures 13 and 14 show satisfactory agreement in terms of pit depth, pit aspect ratio and pit geometry. The results demonstrate that the model is appropriately validated and is able to simulate the evolution of pit characteristics during pitting corrosion damage.

5.2. Influence of corrosion and diffusion processes on pit propagation behaviour

Localised corrosion is a complex stochastic process in which the kinetics can be affected by several mechanisms including metal dissolution, diffusion of corrosion species, and hydrolysis. The CA model simulating non-flow conditions with optimized parameters was employed to investigate the influence of (i) oxidation of metal to Fe^{2+}, (ii) hydrolysis of Fe^{2+}, and (iii) accumulation of corrosion products ($Fe(OH)_2$ and $Fe(OH)_3$) in the pit, on the evolution of maximum pit depth with time. This was achieved by varying each of these three parameters while keeping other parameters given in Table 3 constant.

5.2.1. Influence of oxidation of metal

Activation controlled corrosion has been shown to depend on the rate of oxidation of metal atoms to cations that participate in redox reactions. The probability of corrosion, *P_corr*, was incorporated into the model to simulate the rate of oxidation of the metal (Fe) to Fe^{2+}. Figure 15 shows a power law relationship between maximum pit depth and time. The empirical power law relationship has been previously observed in pitting corrosion studies [32] and is generally used to model pit growth rate in metallic alloys [12, 79]. It is also observed from Figure 15 that at a given time, maximum pit depth increases as *P_corr* increases. Higher probability for corrosion increases both the tendency for oxidation and the concentration of the corrosion species, Fe^{2+} within the pit. Consequently the rates of metal dissolution and pit growth will increase. Changes in the value of *P_corr* reflect factors such as potential

[80], temperature [81], applied stress [82] and inhibition [83]. These results illustrate the time-dependent nature of localised corrosion damage and the characteristic role of metal dissolution rates in the process.

5.2.2. Influence of accumulation of corrosion products

The mass transport of corrosion products away from the pit site during pit growth, as observed experimentally (Figure 6), can be an important factor controlling stable pit growth. An accumulation factor, *Sed*, was incorporated into the model to account for the rate of accumulation of corrosion products ($Fe(OH)_2$ and $Fe(OH)_3$) in the pit during localised dissolution. Figure 16 shows the evolution of maximum pit depth and pit volume with time at different *Sed* values. It can be observed that relatively higher values of *Sed* result in lower values of maximum pit depth and pit volume at any given time. This indicates that an increase in the rate of mass transport of corrosion products, simulated by decrease in the value of *Sed*, increases the rate of damage by increasing metal loss and pit growth rates. One process by which the accumulation of corrosion products can limit corrosion rates is through diffusion control, whereby a diffusion barrier is created between the reactant species taking part in the corrosion process [84, 85], in this case, Fe^{2+} and acidic sites.

In a real system, lower *Sed* values may be due to (i) an increase in flow rates wherein corrosion products are transported away from within the pit thus reducing the degree of sedimentation and therefore facilitating electrochemical reactions (increased mass transport) and metal dissolution and, (ii) the local acidification due to hydrolysis of metal ions within the pit, leading to an increase in the solubility of corrosion products thereby also decreasing their rate of accumulation (sedimentation).

5.2.3. Influence of metal ion hydrolysis

Figure 17 shows that the overall damage (maximum pit depth and metal loss) is lowest when *P_Hyd1* is highest. The result of an increase in *P_Hyd1*, i.e. increase in the rate of hydrolysis of Fe^{2+}, on corrosion behaviour is two-fold, as can be seen in Equation 3. One effect is that of increased rates of pit acidification by facilitating the production of acidic sites, thus increasing metal dissolution and pit growth rates. The other effect is that of an increase in the rate of formation of corrosion product ($Fe(OH)_2$), which if accumulated over time, will result in lower metal dissolution rates, as discussed in the previous section. The competition between these two mechanisms during the pit growth determine the rate of propagation

of the pit. The effect of increase in pit acidification rate can be seen in Figure 17 for *P_Hyd1* of 0.01, where the pit depth appears to have a linear relationship with time. The plots suggest that the rate of pit growth is dominated by the rate of hydrolysis of Fe^{2+}, as the rate of formation of corrosion products is not significant to the extent where sedimentation can have appreciable effect. However, as the rate of hydrolysis increases from *P_Hyd1* of 0.1 to 0.3, corrosion product formation rate increases so that sedimentation can influence the pit growth rate.

5.3. Time-evolution of stress and strain distribution around pits

The evaluation of local mechanical conditions around a growing corrosion pit, in a stressed component, is challenging because of the impracticability of analysing stress and strain distributions at every instant during growth, combined with the irregularity of the pit geometry, which can lead to local 'micro-pits' within the pit. Furthermore, dynamic plastic strain, which plays an important role in determining the conditions required for crack initiation, may be induced by the plastic wake left by the pit during growth [86]. Current approaches being employed to evaluate stress and strain distribution around pits are based on a discretised approach whereby a pit is analysed at different time intervals during pit growth [86-88]. However, there is a computational limitation on the number of pit size increments that can be simulated, and therefore some assumptions regarding pit shape have to be made. Figure 18 and 19 respectively show the distribution of Von Mises stress and maximum principal strain around a pit in a direction parallel to loading, at different time intervals. While local strain generally increased with pit depth and pit aspect ratio, both of which increase with time, the effective stress was not observed to increase significantly beyond the yield strength of the material. It is also confirmed, from Figures 17 and 18 that the distribution of strain on the pit surface is not uniform, as reported in other studies [57, 86, 88], but rather it is localised around features that may be described as 'micro-pits'. From a mechanics based viewpoint, these high strain concentration regions may facilitate the conditions for crack initiation. However, in a three-dimensional pit, this will depend on the states of stress and strain and surface constraint compared to the sub-surface material. These results demonstrate that the CAFE model is a reasonable simulation and evaluation method, in real time, of the induced dynamic local stress and strain irrespective of depth and aspect ratio of a growing pit. Moreover, no assumptions are required concerning changes in

depth and geometry. This capability of the CAFE model may prove useful for the realistic assessment of the severity of pits and the prediction of the conditions that facilitate the initiation of cracks from pits.

5.4. Influence of stress on pit propagation behaviour

The result presented in Figure 20 demonstrates that the model is capable of simulating stress-assisted pit growth. The observation that at any given time, the pit depth is greater under applied stress than when there is no stress, and that the difference between the trends in the pit depth-time data obtained, with and without stress, progressively widens as the pit becomes deeper, are consistent with the experimental data. It was particularly noted that the period when the effect of strain localisation on pit growth became significant coincided with the onset of the development of plastic strain around the pit, indicating that elastic strain around the pit had minimal effect on pit growth. The plastic strain in the pit region was evaluated from the Equivalent Plastic Strain (defined as PEEQ in the Abaqus® result database) contour plot to be approximately 0.08 %. This is in agreement with previous investigations on deformation-corrosion interactions where it was reported that anodic dissolution is more dependent on plastic deformation than elastic deformation [75, 89, 90]. From investigations on the influence of surface deformation on corrosion, Akid and Dmytrakh observed characteristic changes in the slopes of corrosion potential, polarisation resistance and Tafel constants of steel in sea water when deformation transitions from the elastic to the plastic regimes [55]. Despic and co-workers [90] observed that, under potentiostatic control, anodic current increased markedly at the onset of plasticity whereas, in the elastic region of the test material, there was no change. It was recently demonstrated that the free energy increment associated with elastic strain is not sufficient to influence the metal dissolution rate [89]. The present results appear to show that the effect of stress on pit growth is attributable to the mechanical-electrochemical effect of the local deformation induced around a pit. This facilitates the anodic dissolution process and consequently the rate of pit growth.

6. Conclusions

A cellular automata finite element model has been developed and employed for simulating stress-assisted pit growth. The proposed approach which allows the incorporation of (i) key electrochemical processes that control pit propagation kinetics, (ii) localised mechanical deformation around a pit, and (iii)

interactions between the two, provides an acceptable physical basis for modelling damage evolution under the combination of aggressive environment and mechanical loading. The model was employed to evaluate the influence of different electrochemical parameters and applied stress on the evolution of depth, aspect ratio and morphology of pits, as a function of time. Qualitatively and quantitatively comparison of simulation results with experimental measurements show that both are in good agreement and that the proposed hybrid model is capable of simulating stress-assisted pitting damage during the pre-crack stages of environment assisted cracking.

Acknowledgements

The authors acknowledge BP for funding this research work under the Facilities Technology Flagship Programme and for providing the test material. The authors would also like to acknowledge Dr C. Evans of BAE Systems, UK for developing the experimental test microcell. S.L. acknowledges support from the Erwin Schrödinger International Institute for Mathematics and Physics (ESI), Vienna. We thank the School of Materials and Corrosion and Protection Centre of the University of Manchester, UK and the Materials and Engineering Research Institute of Sheffield Hallam University, UK for the use of testing facilities.

References

[1] G.S. Chen, K.C. Wan, M. Gao, R.P. Wei, T.H. Flournoy, Transition from pitting to fatigue crack growth—modeling of corrosion fatigue crack nucleation in a 2024-T3 aluminum alloy, Mat. Sci. & Eng. A 219 (1996) 126-132. https://doi.org/10.1016/s0921-5093(96)10414-7

[2] Y. Wang, R. Akid, Role of Nonmetallic Inclusions in Fatigue, Pitting, and Corrosion Fatigue, Corros. 52 (1996) 92-102. https://doi.org/10.5006/1.3292108

[3] S.I. Rokhlin, J.Y. Kim, H. Nagy, B. Zoofan, Effect of pitting corrosion on fatigue crack initiation and fatigue life, Eng. Frac. Mech. 62 (1999) 425-444. https://doi.org/10.1016/s0013-7944(98)00101-5

[4] T.A. Zhou, Influence of pitting on the fatigue life of a turbine blade steel, Fat. Frac. Eng. Mat. & Struc. 22 (1999) 1083-1093. https://doi.org/10.1046/j.1460-2695.1999.00226.x

[5] E.J. Dolley, B. Lee, R.P. Wei, The effect of pitting corrosion on fatigue life, Fat. Frac. Eng. Mat. & Struc. 23 (2000) 555-560.

[6] K.K. Sankaran, R. Perez, K.V. Jata, Effects of pitting corrosion on the fatigue behavior of aluminum alloy 7075-T6: modeling and experimental studies, Mat. Sci. & Eng. A 297 (2001) 223-229.

[7] K. Jones, D.W. Hoeppner, Pit-to-crack transition in pre-corroded 7075-T6 aluminum alloy under cyclic loading, Corros. Sci. 47 (2005) 2185-2198.

[8] B.M. Schonbauer, S.E. Stanzl-Tschegg, A. Perlega, R.N. Salzman, N.F. Rieger, S. Zhou, A. Turnbull, D. Gandy, Fatigue life estimation of pitted 12% Cr steam turbine blade steel in different environments and at different stress ratios, Int. J. Fatigue 65 (2014) 33-43.

[9] H.H. Strehblow, Mechanisms of pitting corrosion: Corrosion mechsnisms in theory and practice, Marcel Dekker Inc., New York, 1995.

[10] L.L. Shreie, R.A. Jarman, C.T. Burstien, Corrosion-Metal/environmental reactions, 3rd ed., Butterworth & Heinemann, Oxford, 1994.

[11] P. Marcus, J. Oudar, Corrosion mechanisms in theory and practice, Marcel Dekker Inc., New York, 1995.

[12] Z. Szklarska-Smialowska, Pitting Corrosion of Metals, National Association of Corrosion Engineers, 1986.

[13] S. Papavinasam, W. Friesen, R. Revie, A. Doiron, Predicting Internal Pitting Corrosion of Oil and Gas Pipelines: A Corrosion Engineering Approach in: NACE Corros. Conf. (2005) 1-17.

[14] Z. Xia, K.C. Chou, Z. Szklarska-Smialowska, Pitting corrosion of carbon steel in CO_2 - containing NaCl Brine, Corros. 45 (1989) 636-642.

[15] C.A. Palacios, J.R. Shadley, Characteristics of Corrosion Scales on Steels in a Col-Saturated NaCI Brine, Corros. 47 (1991) 122-127.

[16] J. Han, S. Nesic, Y. Yang, B.N. Brown, Spontaneous passivation observations during scale formation on mild steel in CO2 brines, Elect. Acta 56 (2011) 5396-5404.

[17] S. Papavinasam, A. Doiron, R. Revie, Model to Predict Internal Pitting Corrosion of Oil and Gas Pipelines, Corros. 66 (2010) 1-11.

[18] M. Karami, Review of Corrosion Role in Gas Pipeline and Some Methods for Preventing it, J. of Press. Vess. Tech. 134 (2012) 54501-54501.

[19] J. Han, Y. Yang, B. Brown, S. Nesic, Electrochemical Investigation of Localized CO2 Corrosion on Mild Steel, NACE Corros. Conf. (2007).

[20] Z. Szklarska-Smialowska, Pitting corrosion of aluminum, Corros. Sci. 41 (1999) 1743-1767.

[21] G.S. Frankel, Pitting Corrosion of Metals A Review of the Critical Factors, J. Electrochem. Soc. 145 (1998) 2186-2198.

[22] E. McCafferty, Sequence of steps in the pitting of aluminum by chloride ions, Corros. Sci. 45 (2003) 1421-1438.

[23] I.A. Chaves, R.E. Melchers, Pitting corrosion in pipeline steel weld zones, Corros. Sci. 53 (2011) 4026-4032.

[24] V. Vignal, N.M. andC. Valot andR. Oltra, L. Coudreuse, Influence of Elastic Deformation on Initiation of Pits on Duplex Stainless Steels, Electrochem. & Solid Stat. Let. 7 (2004) c39-c42.

[25] M.A. Baker, J.E. Castle, The initiation of pitting corrosion of stainless steels at oxide inclusions, Corros. Sci. 33 (1992) 1295-1312.

[26] J.N. Harb, R.C. Alkire, Transport and Reaction during Pitting Corrosion of Ni in 0.5M NaCl: I . Stagnant Fluid, J. Elect. Soc. 138 (1991) 2594-2600.

[27] S.M. Sharland, A mathematical model of crevice and pitting corrosion-II. The mathematical solution, Corros. Sci. 28 (1988) 621-630.

[28] R. Reigada, F. Sagués, J.M. Costa, A Monte Carlo simulation of localized corrosion, J. Chem. Phys. 101 (1994) 2329-2337.

[29] K.V.S. Ramana, T. Anita, S. Mandal, S. Kaliappan, H. Shaikh, P.V. Sivaprasad, R.K. Dayal, H.S. Khatak, Effect of different environmental parameters on pitting behavior of AISI type 316L stainless steel: Experimental studies and neural network modeling, Mat. & Des. 30 (2009) 3770-3775.

[30] J. Rajasankar, N.R. Iyer, A probability-based model for growth of corrosion pits in aluminium alloys, Eng. Frac. Mech. 73 (2006) 553-570.

[31] D.R. Gunasegaram, M.S. Venkatraman, I.S. Cole, Towards multiscale modelling of localised corrosion, Int. Mat. Rev. 59 (2014) 84-114.

[32] S. Ishihara, S. Saka, Z.Y. Nan, T. Goshima, S. Sunada, Prediction of corrosion fatigue lives of aluminium alloy on the basis of corrosion pit growth law, Fat. Frac. Eng. Mat. & Struc. 29 (2006) 472-480.

[33] Y. Kondo, Prediction of Fatigue Crack Initiation Life Based on Pit Growth, Corros. 45 (1989) 7-11.

[34] A. Turnbull, Review of modelling of pit propagation kinetics, Brit. Corros. J. 28 (1993) 297-308.

[35] A. Turnbull, Theoretical Evaluation of the Dissolved Oxygen Concentration in a Crevice or Crack in a Metal in Aqueous Solution, Corros. Eng. Sci. Tech. 15 (1980) 162-171.

[36] S.M. Sharland, A review of the theoretical modelling of crevice and pitting corrosion, Corros. Sci. 27 (1987) 289-323.

[37] B. Malki, B. Baroux, Computer simulation of the corrosion pit growth, Corros. Sci. 47 (2005) 171-182.

[38] M.K. Cavanaugh, R.G. Buchheit, N. Birbilis, Modeling the environmental dependence of pit growth using neural network approaches, Corros. Sci. 52 (2010) 3070-3077.

[39] S. Wolfram, Statistical mechanics of cellular automata, Rev. Modern Phys. 55 (1983) 601-644.

[40] H. Chen, Y. Chen, J. Zhang, Cellular automaton modeling on the corrosion/oxidation mechanism of steel in liquid metal environment, Prog. Nucl. Energ. 50 (2008) 587-593.

[41] P. Cordoba-Torres, R.P. Nogueira, L. de Miranda, L. Brenig, J. Wallenborn, V. Fairén, Cellular automaton simulation of a simple corrosion mechanism: mesoscopic heterogeneity versus macroscopic homogeneity, Elect. Acta 46 (2001) 2975-2989.

[42] L. Berec, Techniques of spatially explicit individual-based models: construction, simulation, and mean-field analysis, Eco. Model. 150 (2002) 55-81.

[43] D. di Caprio, C. Vautrin-Ul, J. Stafiej, J. Saunier, A. Chausse, D. Féron, J.P. Badiali, Morphology of corroded surfaces: Contribution of cellular automaton modelling, Corros. Sci. 53 (2011) 418-425.

[44] H. Wang, E. Han, Simulation of metastable corrosion pit development under mechanical stress, Electrochem. Acta 90 (2013) 128-134.

[45] H. Wang, E.-H. Han, Computational simulation of corrosion pit interactions under mechanochemical effects using a cellular automaton/finite element model, Corros. Sci. 103 (2016) 305-311.

[46] L. Li, X. Li, C. Dong, Y. Huang, Computational simulation of metastable pitting of stainless steel, Electrochem. Acta 54 (2009) 6389-6395.

[47] L. Lei, L. Xiaogang, D. Chaofang, X. Kui, L. Lin, Cellular automata modeling on pitting current transients, Electrochem. Comm. 11 (2009) 1826-1829.

[48] P. Van der Weeen, A.M. Zimer, E.C. Pereira, L.H. Mascaro, O.M. Bruno, B. De Baets, Modeling pitting corrosion by means of a 3D discrete stochastic model, Corros. Sci. 82 (2014) 133-144.

[49] R.M. Pidaparti, L. Fang, M.J. Palakal, Computational simulation of multi-pit corrosion process in materials, Comp. Mat. Sci. 41 (2008) 255-265. https://doi.org/10.1016/j.commatsci.2007.04.017

[50] O. Fatoba, R. Akid, Uniaxial cyclic elasto-plastic deformation and fatigue failure of API-5L X65 steel under various loading conditions, Theor. Appl. Fract. Mech., 94 (2018) 147-159. https://doi.org/10.1016/j.tafmec.2018.01.015

[51] J.N. Harb, R.C. Alkire, The effect of fluid flow on growth of single corrosion pits, Corros. Sci. 29 (1989) 31-43. https://doi.org/10.1016/0010-938x(89)90078-4

[52] P.R. Roberge, Corrosion Engineering: Principles and Practice, McGraw-Hill, 2008.

[53] R. Ebara, Corrosion fatigue crack initiation in 12% chromium stainless steel, Mat. Sci. Eng. A 468–470 (2007) 109-113. https://doi.org/10.1016/j.msea.2006.09.128

[54] J. Ma, B. Zhang, J. Wang, G. Wang, E. Han, W. Ke, Anisotropic 3D growth of corrosion pits initiated at MnS inclusions for A537 steel during corrosion fatigue, Corros. Sci. 52 (2010) 2867-2877. https://doi.org/10.1016/j.corsci.2010.04.036

[55] R. Akid, I.M. Dmytrakh, Influence of surface deformation and electrochemical variables on corrosion and corrosion fatigue crack development, Fat. Frac. Eng. Mat. & Struc. 21 (1998) 903-911.

[56] A. Turnbull, D.A. Horner, B.J. Connolly, Challenges in modelling the evolution of stress corrosion cracks from pits, Eng. Frac. Mech. 76 (2009) 633-640.

[57] D.A. Horner, B.J. Connolly, S. Zhou, L. Crocker, A. Turnbull, Novel images of the evolution of stress corrosion cracks from corrosion pits, Corros. Sci. 53 (2011) 3466-3485.

[58] O. Fatoba, Experimental and modelling studies of corrosion fatigue damage in a linepipe steel, in, PhD Thesis, University of Manchester, UK. 2015.

[59] B.D. Van, G.C. Farrington, C. Laird, The interaction of simultaneous cyclic straining and aqueous corrosive attack in the behavior of persistent slip bands, Acta Metall. 33 (1985) 1593-1600.

[60] MATLAB ® 2013a, Mathworks, 2013.

[61] G.T. Gaudet, W.T. Mo, T.A. Hatton, J.W. Tester, J. Tilly, H.S. Isaacs, R.C. Newman, Mass transfer and electrochemical kinetic interactions in localized pitting corrosion, Americ. Inst. Chem. Eng. J. 32 (1986) 949-958.

[62] G.T. Burstein, P.C. Pistorius, S.P. Mattin, The nucleation and growth of corrosion pits on stainless steel, Corros. Sci. 35 (1993) 57-62.

[63] A. Taleb, A. Chaussé, M. Dymitrowska, J. Stafiej, J.P. Badiali, Simulations of Corrosion and Passivation Phenomena: Diffusion Feedback on the Corrosion Rate, J. Phys. Chem. B 108 (2004) 952-958.

[64] J. Saunier, M. Dymitrowska, A. Chaussé, J. Stafiej, J.P. Badiali, Diffusion, interactions and universal behavior in a corrosion growth model, J. Electroanaly. Chem. 582 (2005) 267-273.

[65] A. Turnbull, The solution composition and electrode potential in pits, crevices and cracks, Corros. Sci. 23 (1983) 833-870.

[66] H.W. Pickering, The significance of the local electrode potential within pits, crevices and cracks, Corros. Sci. 29 (1989) 325-341.

[67] ABAQUS ® Analysis user's manual I-V. Version 6.13, ABAQUS Inc., Dassualt Systemes USA, 2013.

[68] R.J. Selines, R.M. Pelloux, Effect of cyclic stress wave form on corrosion fatigue crack propagation in al-zn-mg alloys, Metall. Trans., 3 (1972) 2525-2531.

[69] Z.F. Wang, J. Li, J.Q. Wang, W. Ke, The influence of loading waveform on corrosion fatigue crack propagation, Corros. Sci., 37 (1995) 1551-1565.

[70] O.M. Romaniv, B.Y. Heneha, O.M. Huta, V.O. Vasylechko, Effect of stresses on the electrochemical corrosion of steel in aqueous media, Mat. Sci., 32 (1996) 760-763.

[71] R. Akid, The role of stress-assited localised corrosion in the development of short fatigue cracks, in: W.A. Van Der Sluys, R.S. Piascik, R. Zawierucha (Eds.) Effects of the environment on the initiation of crack growth, ASTM STP 1298, Americam Society of Testing and Materials (1997) 3-17.

[72] V. Mary, C. Valot, R. Oltra, L. Coudreuse, Influence of Elastic Deformation on Initiation of Pits on Duplex Stainless Steels, Electrochem. Solid Stat. Lett. 7 (2004) C39-C42.

[73] L. Ma, D.W. Hoeppner, The Effects of Pitting on the Fatigue Crack Nucleation in 7075-T6 Aluminium Alloy, in, NASA Conference Publication 425-440.

[74] E.M. Gutman, Mechanochemistry of Materials, Cambridge International Science Publishing, Cambridge, 1998.

[75] E.M. Gutman, G. Solovioff, D. Eliezer, The mechanochemical behavior of type 316L stainless steel, Corros. Sci. 38 (1996) 1141-1145.

[76] M. Sun, K. Xiao, C. Dong, X. Li, P. Zhong, Effect of stress on electrochemical characteristics of pre-cracked ultrahigh strength stainless steel in acid sodium sulphate solution, Corros. Sci. 89 (2014) 137-145.

[77] I.M. Sobol, On the distribution of points in a cube and the approximate evaluation of integrals, USSR Comp. Math. Phys. 7 (1967) 86-112.

[78] K. Beven, J. Freer, Equifinality, data assimilation, and uncertainty estimation in mechanistic modelling of complex environmental systems using the GLUE methodology, J. Hydro. 249 (2001) 11-29.

[79] H.P. Godard, The Corrosion of Light Metals, John Wiley and Sons, 1967.

[80] G.S. Frankel, L. Stockert, F. Hunkeler, H. Boehni, Metastable Pitting of Stainless Steel, Corros. 43 (1987) 429-436.

[81] N. Ebrahimi, M.H. Moayed, A. Davoodi, Critical pitting temperature dependence of 2205 duplex stainless steel on dichromate ion concentration in chloride medium, Corros. Sci. 53 (2011) 1278-1287.

[82] Z.Y. Nan, S. Ishihara, T. Goshima, Corrosion fatigue behavior of extruded magnesium alloy AZ31 in sodium chloride solution, Int. J. Fatig. 30 (2008) 1181-1188.

[83] S.M. Sayed, H.A. el Shayeb, The measurement of pitting corrosion currents of steel in neutral aqueous solutions, Corros. Sci. 28 (1988) 153-162.

[84] F.M. Song, D.W. Kirk, J.W. Graydon, D.E. Cormack, Effect of Ferrous Ion Oxidation on Corrosion of Active Iron under an Aerated Solution Layer, Corros. 58 (2002) 145-155.

[85] E.E. Stansbury, R.A. Buchanan, Fundamentals of Electrochemical Corrosion, ASM International, 2000.

[86] A. Turnbull, L. Wright, L. Crocker, New insight into the pit-to-crack transition from finite element analysis of the stress and strain distribution around a corrosion pit, Corros. Sci. 52 (2010) 1492-1498.

[87] M. Cerit, K. Genel, S. Eksi, Numerical investigation on stress concentration of corrosion pit, Eng. Fail. Analys.16 (2009) 2467-2472.

[88] M. Cerit, Numerical investigation on torsional stress concentration factor at the semi elliptical corrosion pit, Corros. Sci. 67 (2013) 225-232.

[89] B.T. Lu, J.L. Luo, P.R. Norton, H.Y. Ma, Effects of dissolved hydrogen and elastic and plastic deformation on active dissolution of pipeline steel in anaerobic groundwater of near-neutral pH, Acta Mater. 57 (2009) 41-49.

[90] A.R. Despic, R.G. Raicheff, J.O.M. Bockris, Mechanism of the Acceleration of the Electrodic Dissolution of Metals during Yielding under Stress, J. Chem. Phys. 49 (1968) 926-939.

FIGURE CAPTIONS

Fig. 1. Micro-capillary cell set-up with test sample (inset: Metal-electrolyte-capillary tip interface).

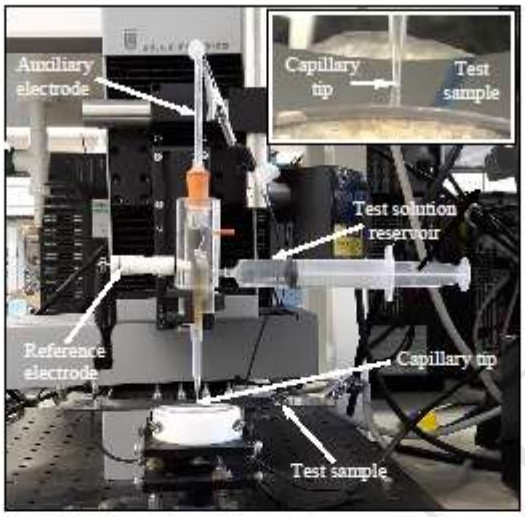

Fig. 2. Schematic of experimental set-up of scanning droplet cell and fatigue test rig for investigating the effect of stress and electrolyte flow on localised corrosion.

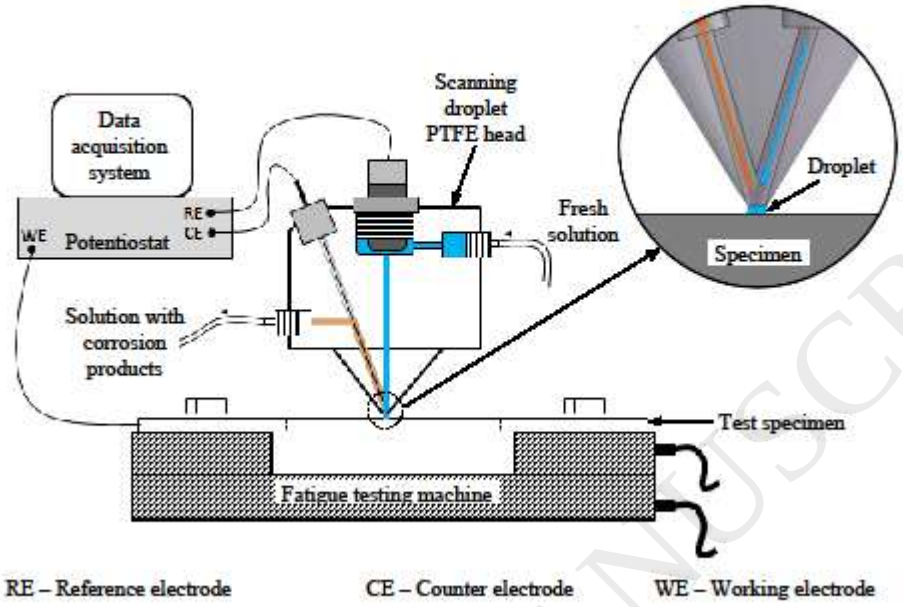

Fig. 3. Dimensions of the fatigue test specimen, illustrating the location of the pit.

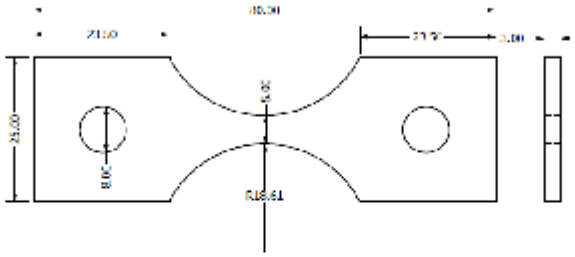

Fig. 4. (a) Optical image of a pit observed on the surface of fatigue specimen after potentiostatic polarisation for 16,000 seconds, and (b) confocal microscopy reconstructed image showing 3-dimensional cross-sectional profile of the pit shown in (a).

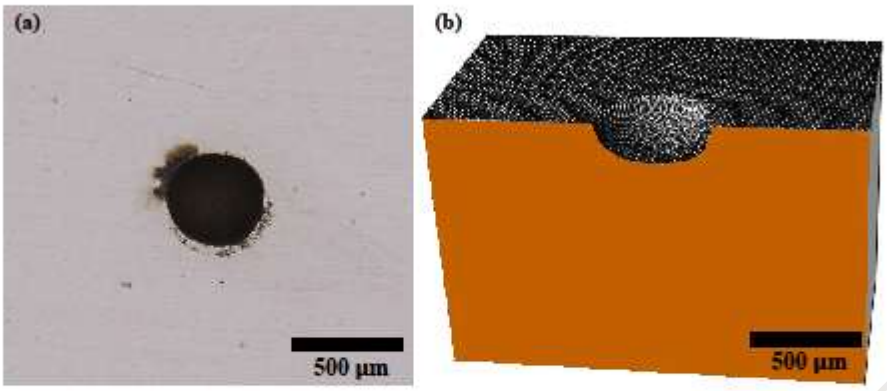

Fig. 5. Time-evolution of pit depth (a) and pit aspect ratio (b) under non-flow and unstressed conditions.

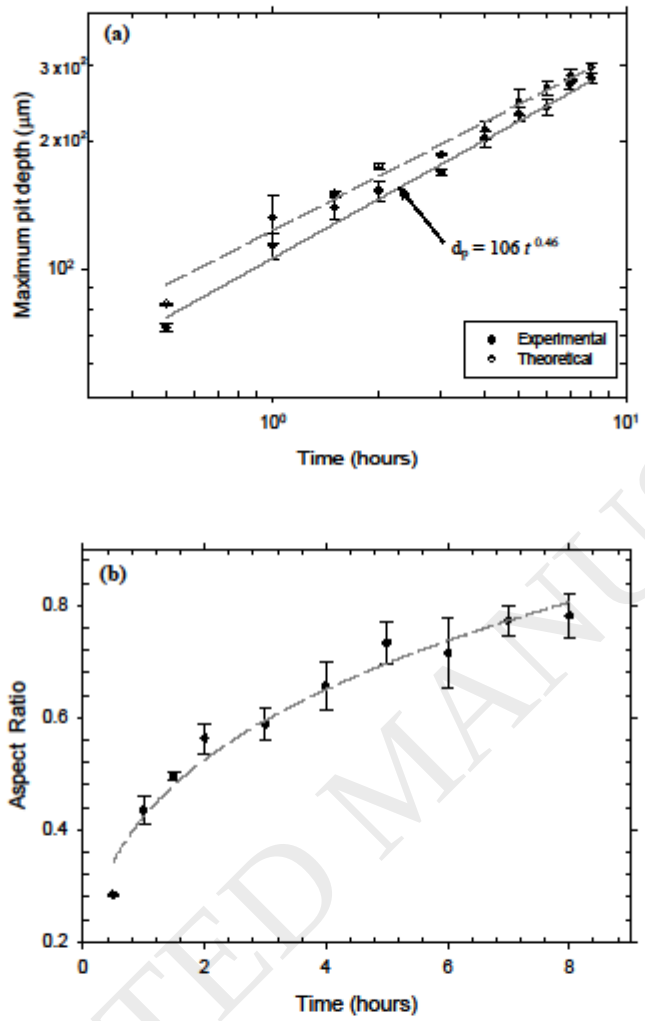

Fig. 6. Time-evolution of pit depth showing the influence of cyclic stress and flowing conditions on pit propagation kinetics. Note that the flow seemed to have greater effect on pit depth than applied stress. (FR - flow rate).

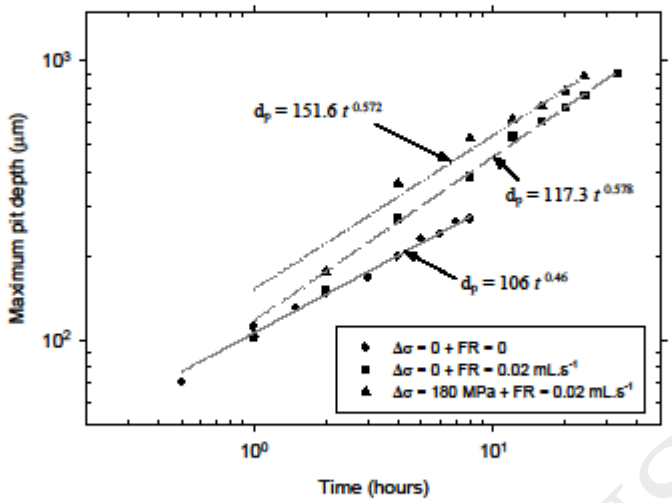

Fig. 7. Schematic showing the cellular automaton finite element model architecture showing the CA and FE components and information flow between them. A – Abaqus ®, M – Matlab ®, P – Python ® (The coloured version of this figure is available online).

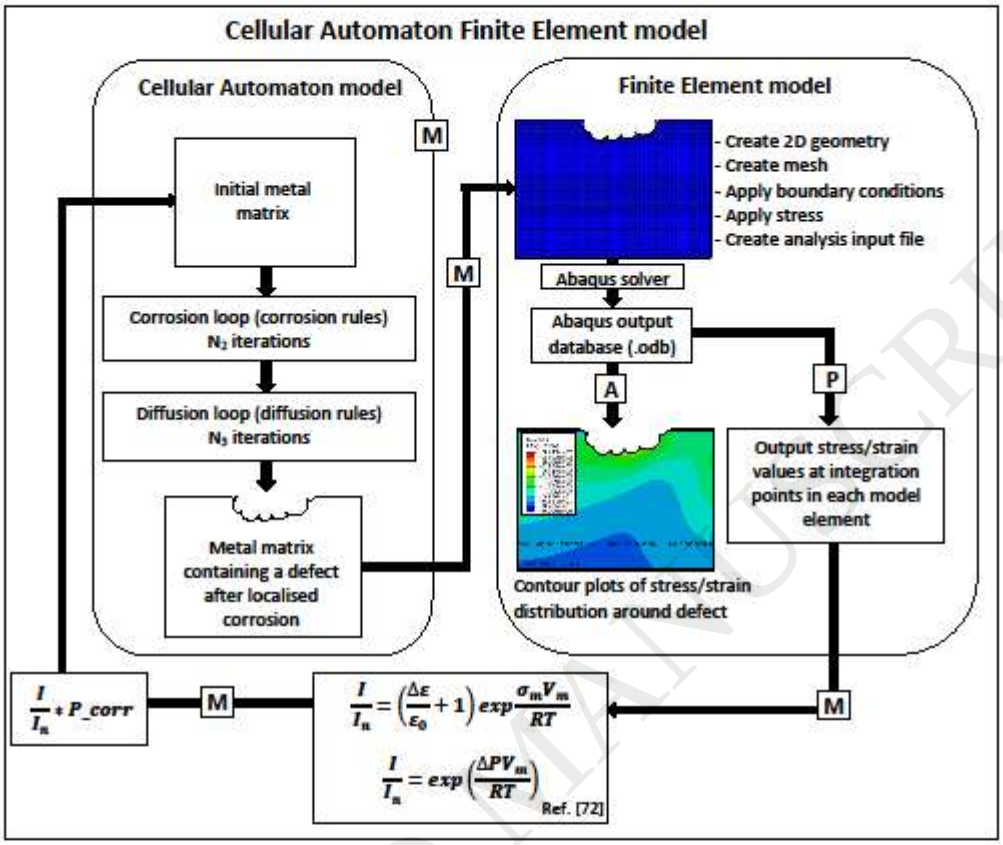

Fig. 8. Metal-electrolyte-capillary configuration showing (a) schematic of localised corrosion in real system, (b) schematic of micro-capillary cell and (c) CA modelling sites of the system in (a).

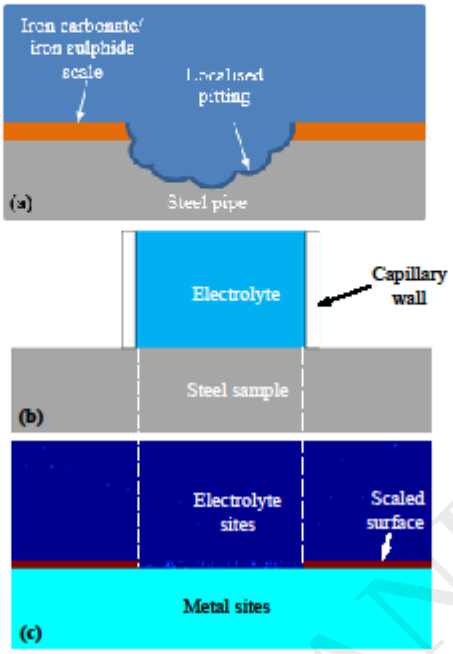

Fig. 9 Schematic of cellular space for cellular automata modelling.

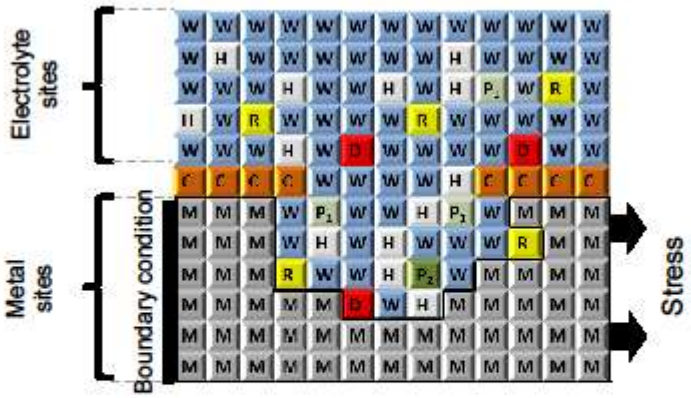

Fig. 10. Moore neighbourhood of range 1.

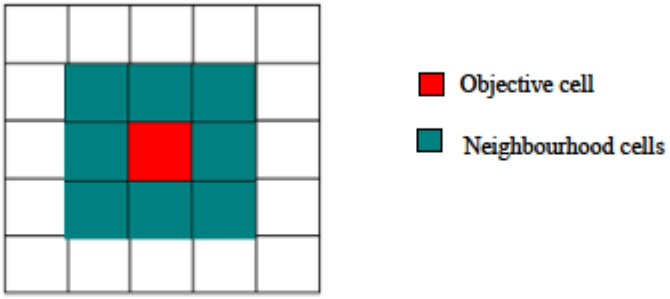

Fig. 11. Corrosion rules used in the CA to simulate (a) oxidation of Fe to Fe^{2+}, (b) oxidation of Fe^{2+} to Fe^{3+}, (c) hydrolysis of Fe^{2+} to $Fe(OH)_2$ and (d) hydrolysis of Fe^{3+} to $Fe(OH)_3$.

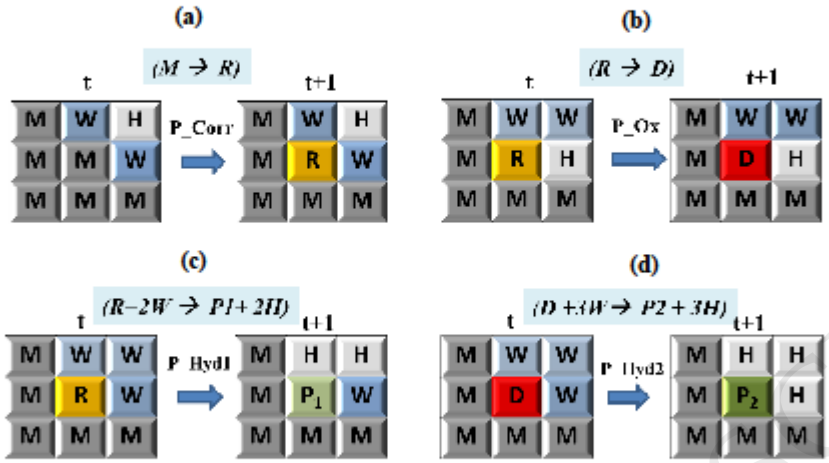

Fig. 12. Diffusion rules used in CA to simulate (a) isotropy (same probability in all the directions for a H site) and (b) precipitation (3rd option is most likely).

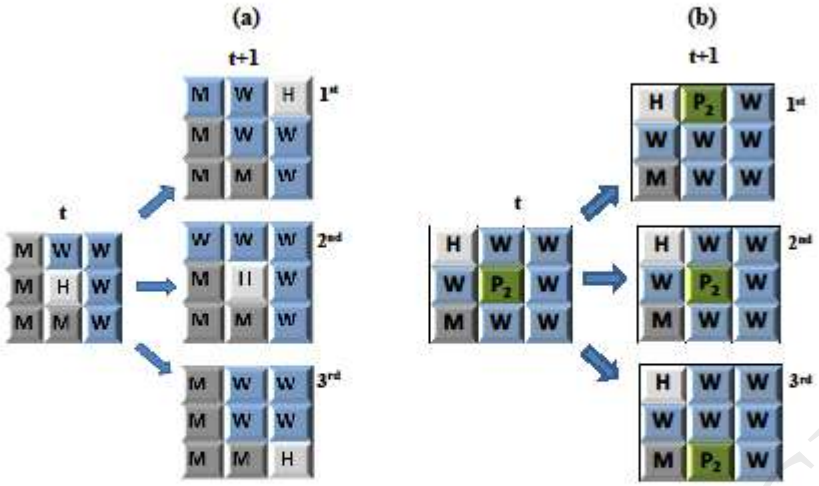

Fig. 13. Simulation results of maximum pit depth as a function of time under (a) non-flow and (b) flowing conditions.

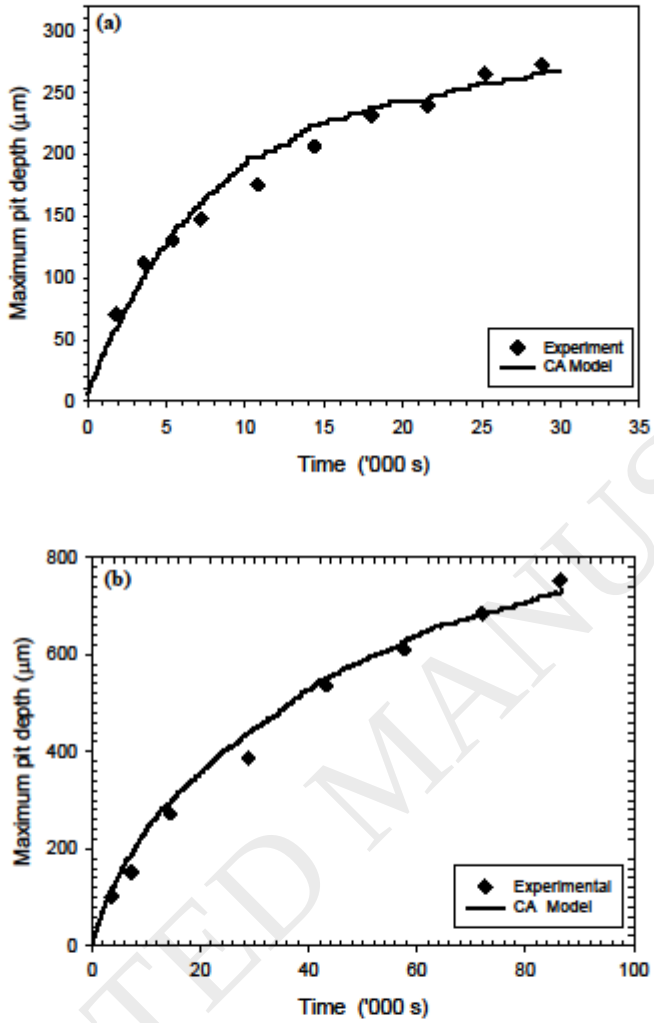

Fig. 14. Comparison between experimental and simulated pit cross-sectional profiles at (a) 1800 (b) 7200 (c) 14400, and (d) 25200 seconds.

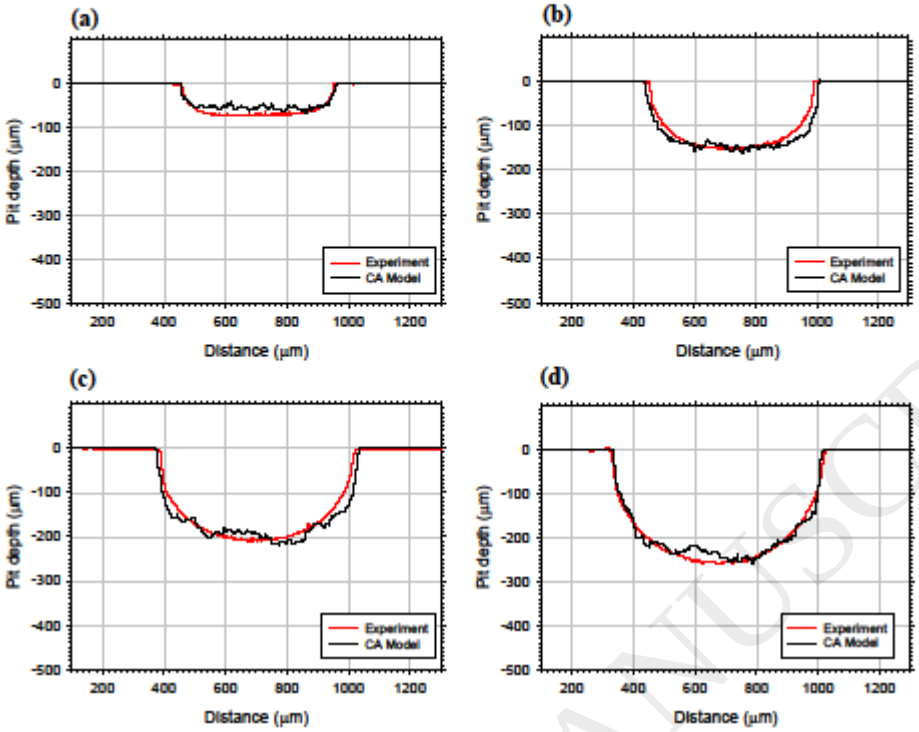

Fig. 15. Influence of metal oxidation on time-dependent evolution of maximum pit depth (The coloured version of this figure is available online).

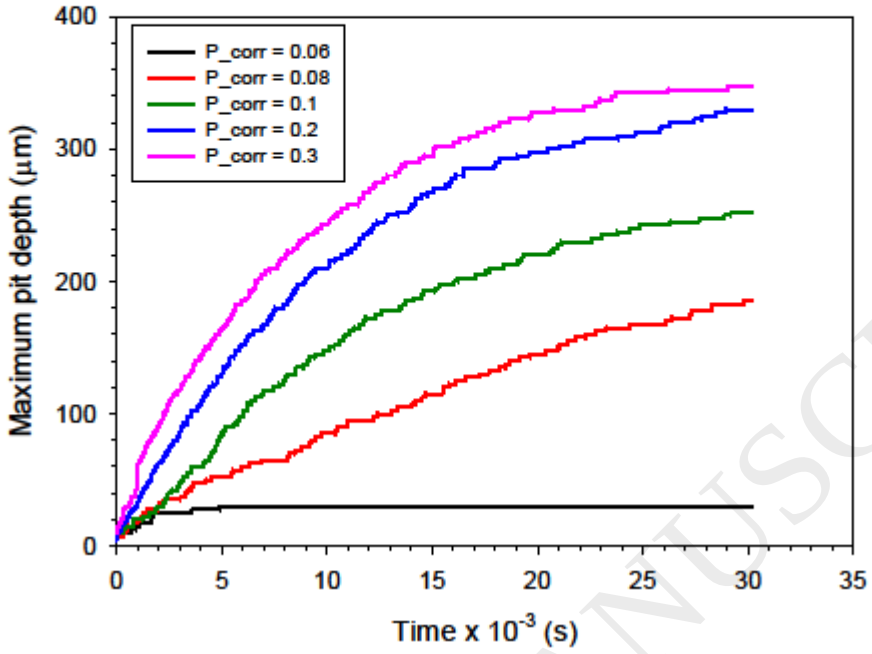

Fig. 16. Influence of corrosion products accumulation on time-dependent evolution of maximum pit depth (The coloured version of this figure is available online).

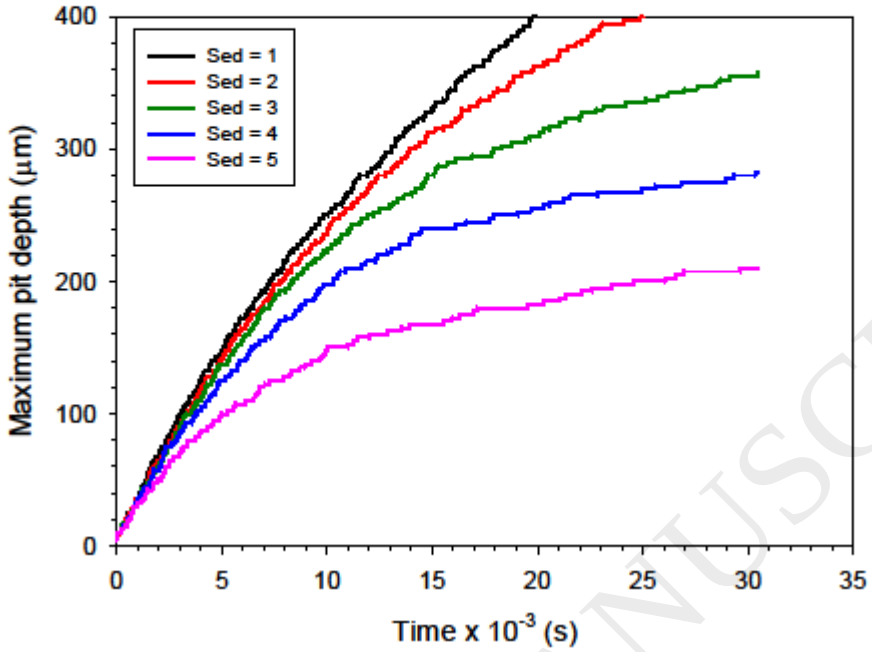

Fig. 17. Influence of metal ion hydrolysis on time-dependent evolution of maximum pit depth (The coloured version of this figure is available online).

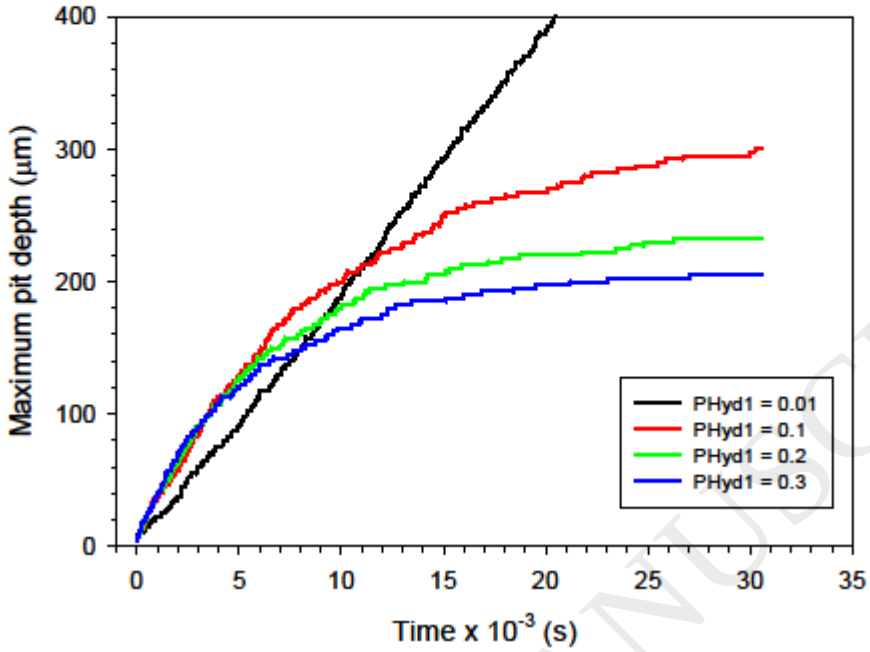

Fig. 18. Evolution and distribution of equivalent stress around a growing pit (σ_{max} = 200 MPa, [A – time: 5400 s, maximum pit depth: 126 µm, aspect ratio: 0.47], [B – time: 10800 s, maximum pit depth: 197 µm, aspect ratio: 0.64], [C – time: 18000 s, maximum pit depth: 242 µm, aspect ratio: 0.73]). Note the stress concentration at the micropits at the bottom of the primary pit. Note also that the applied σ_{max} is the same as

the applied maximum stress during fatigue tests where Δσ = 180 MPa and Stress ratio = 0.1 (The coloured version of this figure is available online).

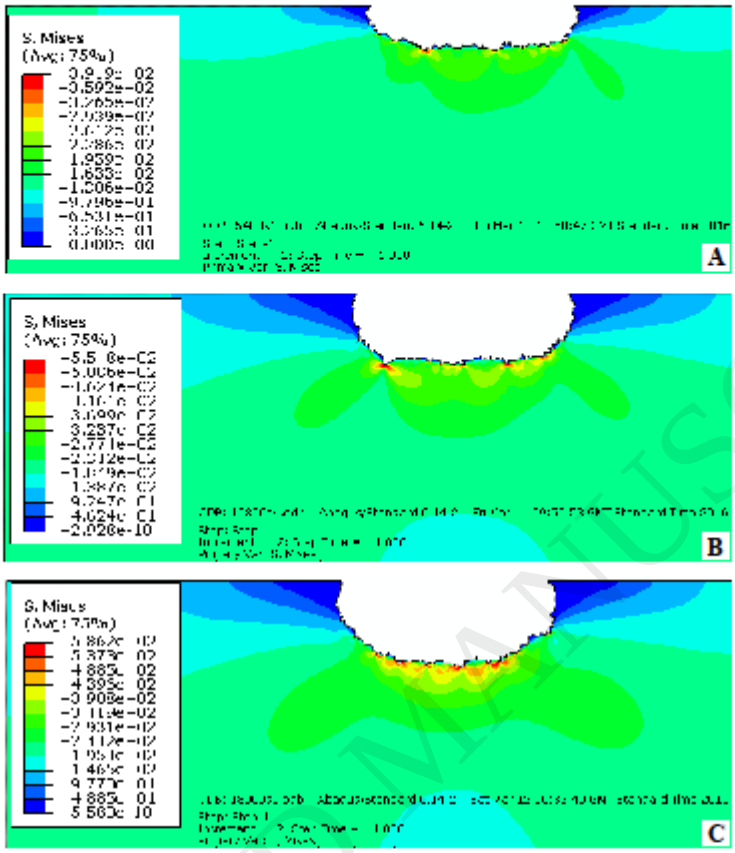

Fig. 19. Evolution and distribution of total strain around a growing pit (σ_{max} = 200 MPa, [A – time: 5400 s, maximum pit depth: 126 µm, aspect ratio: 0.47], [B – time: 10800 s, maximum pit depth: 197 µm, aspect

ratio: 0.64], [C – time: 18000 s, maximum pit depth: 242 μm, aspect ratio: 0.73]). Note the strain concentration at the micropits at the bottom of the primary pit. Note also that the applied σ_{max} is the same as the applied maximum stress during fatigue tests where Δσ = 180 MPa and Stress ratio = 0.1 (The coloured version of this figure is available online).

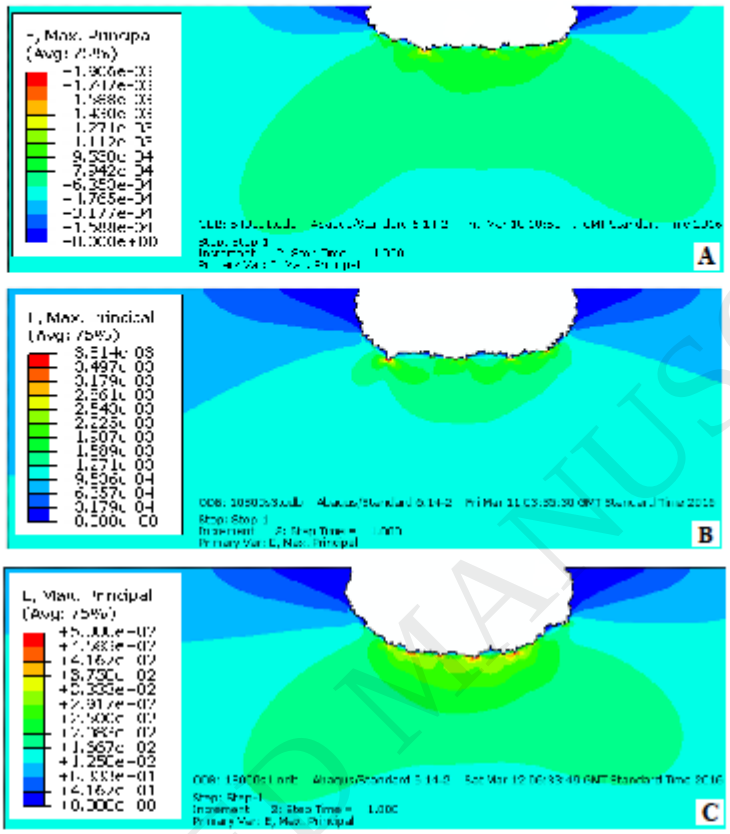

Fig. 20. Evolution of maximum pit depth with time with and without stress at solution flow rate of 0.02 mL.s^{-1}. Note that the applied σ_{max} is the same as the applied maximum stress during fatigue tests where $\Delta\sigma$ = 180 MPa and Stress ratio = 0.1 (The coloured version of this figure is available online).

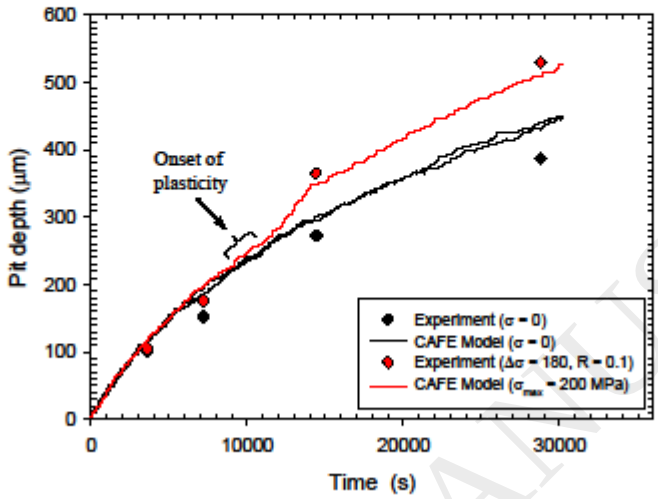

TABLES

Table 1

Chemical composition of API 5L X65 steel (wt%).

C	Si	Mn	P	Mo	V	Cr	Ni	Cu	Nb	Ti	Al	S	Fe
0.05	0.28	1.08	0.01	0.13	0.06	0.07	0.37	0.16	0.027	0.03	0.037	0.001	bal

Table 2

States of the cells in the cellular automata model.

Species	Occupancy	Symbol
Neutral solution site	Water	**W**
Acidic solution site	Proton concentration sites	**H**
Iron (Fe) site	Unreactive metal	**M**
Iron (II) ion site	Reactive metal I	**R**
Iron (III) ion site	Reactive metal II	**D**
Iron (II) Hydroxide site	Corrosion product I	**P1**
Iron (III) Hydroxide site	Corrosion product II	**P2**
Capillary wall site	Capillary surface	**C**

Table 3

Summary of probabilities obtained for optimized model under flow and non-flow solution conditions.

Probability	Non-flow	With Flow
P_corr	0.23	0.26
P_ox	0.28	0.32
P_Hyd1	0.15	0.15
P_Hyd2	0.30	0.30
P_diffH *	0.50	0.50
P_diffFeHyII	0.06	0.06
P_diffFeHyIII	0.06	0.06
Sed	3.30	1.12

*The values for P_diffH, P_diffFe^{2+} and P_diffFe^{3+} are equal due to the assumed isotropy condition.